

Topological protection of continuous frequency entangled biphoton states

Zhen Jiang, Yizhou Ding, Chaoxiang Xi, Guangqiang He*, Chun Jiang*

*State Key Laboratory of Advanced Optical Communication Systems and Networks,
Shanghai Jiao Tong University, Shanghai 20040, China*

* gqhe@sjtu.edu.cn, cjiang@sjtu.edu.cn

Abstract

Topological quantum optics that manipulates the topological protection of quantum states has attracted special interests in recent years. Here we demonstrate valley photonic crystals implementing topologically protected transport of the continuous frequency entangled biphoton states. We numerically simulate the nonlinear four-wave mixing interaction of topological valley kink states propagating along the interface between two valley photonic crystals. We theoretically clarify that the signal and idler photons generated from the four-wave mixing interaction are continuous frequency entangled. The numerical simulation results imply that the entangled biphoton states are robust against the sharp bends and scattering, giving clear evidence of topological protection of entangled photon pairs. Our proposal paves a concrete way to perform topological protection of entangled quantum states operating at telecommunication wavelengths.

Introduction

Topological insulators, striking paradigms that implement the insulating bulk and conducting edge, have prompted the contexts of condensed matter physics. Photonic analogue of topological insulators emulating quantum Hall effect in two-dimensional (2D) photonic systems were first demonstrated by Haldane and Raghu^{1,2}. Topological insulators embedding the breaking of time-reversal symmetry require the application of static or synthetic magnetic fields. Subsequently, a profound topological model preserving time-reversal symmetry which is identified by quantum spin Hall (QSH) insulators has been employed³⁻⁵ in photonic systems. Photonic QSH insulators that support topologically protected edge states at the interface between two distinct topologies have been manipulated either theoretically or experimentally⁶⁻⁸. Recent researches have exploited⁹⁻¹² a new concept of topological phases, referring to the quantum valley Hall (QVH) effect. Valley pseudospins, recognized as a degree of freedom, is a promising platform to realize topologically protected transport in photonic devices. It has been experimentally implemented¹³⁻¹⁷ that topological kink states can be conducted at the interface between regions with two distinct valley topologies. The valley kink states show topological nontrivial performances such as back-scattering suppression and robustness against imperfections and disorders.

1 Inspired by advanced behaviors of topological protection, researchers are focusing
2 on exploiting the concepts of topology in the fields of nonlinear and quantum optics.
3 Topological physics provides new exciting aspects of nonlinear optics. For instance,
4 topological protected third-harmonic generation has been experimentally realized¹⁸ in
5 photonic topological metasurfaces emulating the QSH effect. Moreover, a
6 configuration of the graphene metasurface imitating the quantum Hall effect
7 theoretically proves¹⁹ that the four-wave mixing (FWM) is topologically protected with
8 the breaking of time-reversal symmetry. Most recently, the combination of topological
9 edge states and quantum optics gives rise to potential applications for quantum
10 communication, such as a topological quantum source²⁰, topological single quantum
11 emitters²¹, topological biphoton quantum states^{22,23}, [topologically protected quantum](#)
12 [interference](#)²⁴ and even quantum entanglement²⁵. The aforementioned nonlinear and
13 topological quantum photonic devices may provide a manipulated platform for on-chip
14 nonlinear manipulation or quantum information processing.

15 Here we demonstrate topologically protected entangled biphoton states generated
16 from the nonlinear spontaneous FWM process in photonic crystals emulating the QVH
17 effect. We exploit the linear dispersion relations of valley kink states and [explore](#) the
18 transmittances of kink states in the valley photonic crystals (VPCs). Idler photons
19 generated from the FWM process propagating along the topological interfaces are
20 observed due to the emergence of the nonlinear FWM interaction in the configurations.
21 We theoretically clarify the continuous frequency entanglement of generated photon
22 pairs. Quantum optical properties such as the joint spectral amplitude (JSA), Schmidt
23 coefficients, and the entropy of entanglement for biphoton states generated in VPC
24 waveguides are [calculated](#). A remarkable motivation for transferring topological
25 protection into quantum optics is to implement topologically protected quantum states.
26 We numerically simulate the robustness of entangled biphoton states propagating along
27 the interface with sharp bends. The results reveal that edge states of the pump, signal
28 and idler are robust to the sharp bends due to the overlap between the frequencies of
29 FWM interactions and operation bandwidths of valley kink states. The photonic
30 systems supporting topologically protected entangled photon pairs may provide a
31 prospective paradigm for guiding quantum information in on-chip quantum photonics.

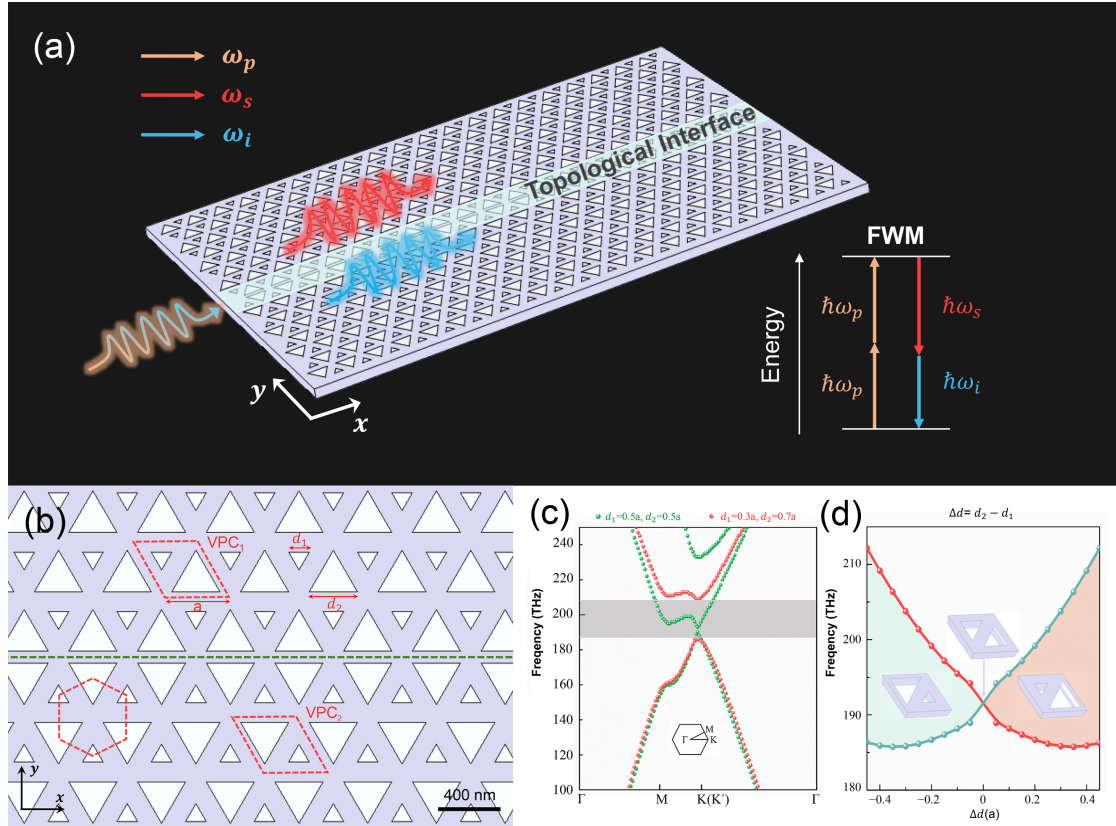
32 **Result**

33 **Topological VPCs**

34 With the advent of all-dielectric VPCs, topological valley kink states become a practical
35 way to protect nonlinear FWM processes in on-chip valley Hall topological insulators.
36 We demonstrate a scheme of silicon-based VPCs implementing robust one-way light
37 transport along the topological interface, as shown in Fig. 1(a). The photonic design
38 comprises equilateral triangular nanoholes with honeycomb lattices possessing C_6
39 symmetry. With the excitation of the source at the pump frequency ω_p , a nonlinear
40 spontaneous FWM process emerges due to the intrinsic third-order nonlinearity of
41 silicon, leading to the generation of correlated signal and idler photons which
42 correspond to the angular frequencies ω_s and ω_i , respectively. As described in the
43 inset, the energy conversion of the FWM processes satisfies $2\hbar\omega_p = \hbar\omega_s + \hbar\omega_i$. With

1 optimized parameters of VPCs, the frequencies of pump, signal and idler photons are
 2 all localized inside the operation bandwidth of topological valley kink states.
 3 Topological protected transport of pump, signal and idler photons can be manipulated
 4 along the the topological interface.

5 We first study the linear topological nature of VPCs, as depicted in Fig. 1(b), the 2D
 6 close-up image of proposed scheme is composed of two different VPCs with parity-
 7 inversed lattices, referred to as VPC₁ and VPC₂. The lattice constant of each unit cell
 8 regarded as a , nanohole sizes are defined as d_1 and d_2 , respectively. The
 9 corresponding band structure of VPC is plotted in Fig. 1(c), for ordinary unit cells ($d_1 =$
 10 $d_2 = 0.5a$), there exist degenerate Dirac cones (at the K and K' valleys) due to the
 11 C_6 lattice symmetry, as displayed by green dots in Fig. 1(c). With the deformation of
 12 the unit cell ($d_1 = 0.3a$, $d_2 = 0.7a$), the C_6 lattice symmetry of VPC reduces to C_3
 13 lattice symmetry, leading to the emergence of a topological photonic bandgap at the K
 14 (K') point in the first Brillouin zone¹⁶, as illustrated by red dots in Fig. 1(c). By
 15 calculating the integration of Berry curvatures over the Brillouin zone, the valley Chern
 16 numbers of VPCs are given by $C_{K/K'} = \pm 1/2$ ^{9,10,15,16}. Therefore, the valley Chern
 17 number of the system composed of VPC₁ and VPC₂ is calculated as $|C_{K/K'}| = 1$,
 18 resulting in topological nontrivial nature of VPCs^{15,16}. To quantitatively analyze the
 19 topological transition of VPCs, we simulate the evolution of bandgap of VPC with the
 20 function of $\Delta d (\Delta d = d_1 - d_2)$, as visualized in Fig. 1(d). Notably, the sizes of
 21 bandgaps grow with the increasing of Δd .



22 Fig. 1 Diagram of the on-chip VPC topological insulators. (a) Geometry of silicon-based VPCs
 23 implementing topological valley kink states, the inset shows energy conversion of nonlinear FWM
 24

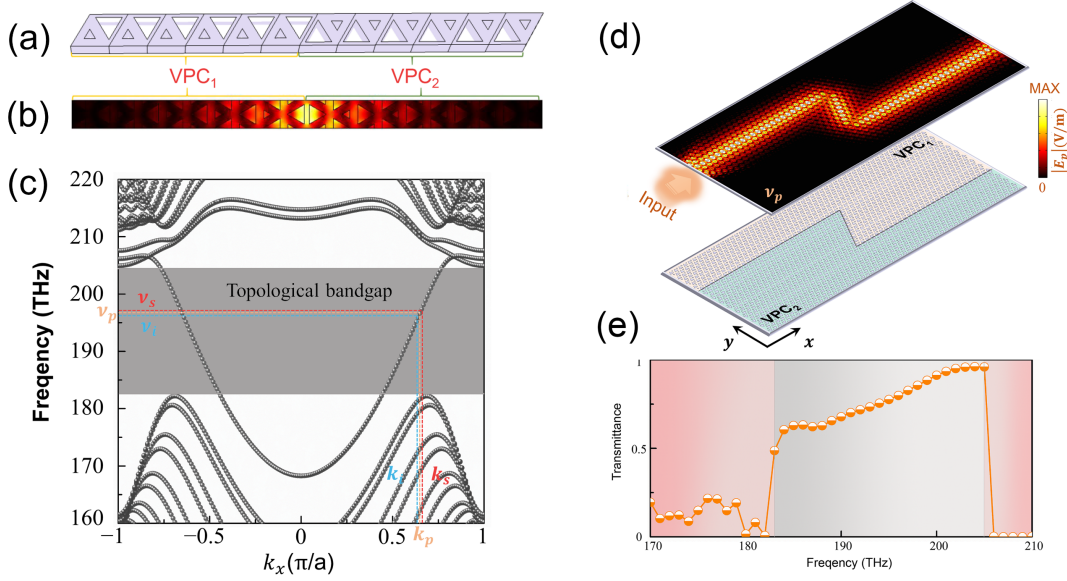
1 process. (b) 2D close-up image of VPCs with lattice constant $a = 410$ nm, green dashed line
 2 denotes the interface between VPC₁ ($d_1 = 0.3a$, $d_2 = 0.7a$) and VPC₂ ($d_1 = 0.7a$, $d_2 = 0.3a$).
 3 (c) Corresponding band structures of VPC where the green and red dots represent the band of
 4 ordinary unit cells ($d_1 = d_2 = 0.5a$) and deformed unit cells ($d_1 = 0.3a$, $d_2 = 0.7a$) respectively.
 5 (d) Diagram of the topological bandgap of VPCs as a function of Δd ($\Delta d = d_1 - d_2$).

6 **Linear response of topological valley kink states**

7 To get more insight into the underlying features of topological valley kink states, we
 8 calculate the dispersion relation of the configuration comprising of VPC₁ and VPC₂ (Fig.
 9 2(a)). As illustrated in Fig. 2(c), there exists a pair of valley-dependent edge modes
 10 localized inside the topological bandgap, and the dispersion curves with opposite slopes
 11 indicates the opposite propagation directions of two kink states. In other words, the
 12 propagating direction of kink states locks to valleys, which refers to as “valley-locked”
 13 chirality²⁶. Noticeably, the dispersion slope is virtually linear, which provides a
 14 convenient method to design the nonlinear spontaneous FWM process. For pragmatic
 15 consideration, we choose pump frequency $\nu_p = 196.5$ THz. Simulated field profiles
 16 of the valley kink state around the interface are displayed in Fig. 2(b).

17 To visualize the topological protection of valley kink states in the VPCs, we perform
 18 the full-wave simulations to study the field distributions along the topological interface
 19 at the pump frequency $\nu_p = 196.5$ THz. We consider a “Z” shaped interface between
 20 the VPC₁ and VPC₂, as shown in Fig. 2(d), we conduct an excitation $E_p = E_x + iE_y$
 21 to emulate a right circularly polarized light. Note that valley-polarized topological kink
 22 states are locked to the circular polarizations of the excited light, with right circularly
 23 polarized light locking to forward-propagating topological kink states, while left
 24 circularly polarized light locking to back-propagating kink states. The simulation result
 25 reveals that electromagnetic wave smoothly flows through sharp corners without visible
 26 back-scattering, which proves that kink states are robust against sharp bends due to the
 27 nature of topological protection. The vortex-like characteristic of excitation only
 28 supports one forward-propagating mode. Therefore, the backward-propagating mode is
 29 suppressed in the QVH system, which is analogous to the pseudospins of helical edge
 30 states in the QSH system^{6,7}. Remarkably, the electric field of the topological valley kink
 31 state is confined at the interface between two different VPCs.

32 We further [explore](#) the transmission spectrum of proposed VPCs with a “Z” shaped
 33 interface, as depicted in Fig. 2(e). The detector dipoles are set around the input and
 34 output port. There exists a distinct peak between 183 THz and 205 THz, which is
 35 consistent with the bandwidth of the topological bandgap in the dispersion relations.
 36 The maximum transmittance is nearly unit in the bandgap, however, a sharp decline of
 37 transmittance appears for the bulk modes due to the reflection and scattering losses. It
 38 is worth mentioning that bulk modes are excited at the corner of the “Z” shape interface
 39 for the kink states at the low-frequency range, leading to undesired loss at the bends.
 40 Therefore, the transmittance of kink states is not unit at the low-frequency range. With
 41 the frequency increasing, the bulk modes cannot be excited because the frequency of
 42 kink states is far away from the frequency of bulk modes corresponding to the
 43 dispersion relations, which leads to the improvement of transmittance.

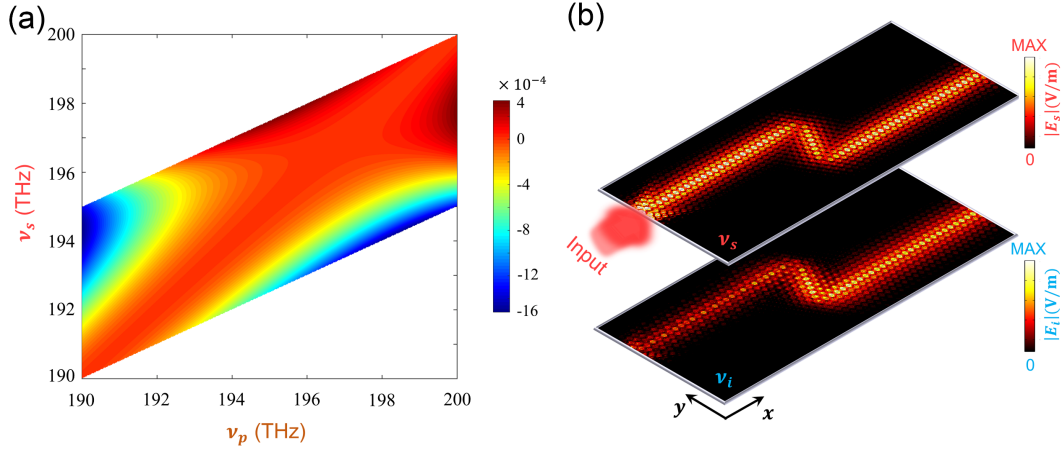


1
2 Fig. 2 Topological valley kink states in photonic crystals emulating QVH effect. (a) Schema of VPC
3 structure comprising of VPC₁ and VPC₂. (b) Simulated field profiles of the valley kink state around
4 the interface. (c) Calculated band diagram of valley kink states for VPC configuration, the gray
5 region denotes the topological bandgap. (d) Field profiles of valley kink states along a “Z” shaped
6 interface between the VPC₁ and VPC₂. (e) Linear transmittances of kink states, the light gray and
7 pink regions represent the bandgap and bulk respectively.

8 Entangled photon pairs of kink states

9 The spontaneous FWM is an efficient nonlinear process for the generation of entangled
10 signal and idler photons. The occurrence of the FWM process is dictated by energy and
11 momentum conversion, satisfying $2\omega_p = \omega_s + \omega_i$ and $2k_p = k_s + k_i$, where k_p ,
12 k_s and k_i are the wavevectors of pump, signal, and idler respectively. With the
13 overlap between the frequencies of FWM interactions and operation bandwidths of
14 topological insulators, topological protection of correlated biphotons²² in addition to
15 frequency-entangled photon pairs²⁵ could be implemented. The dispersion relation of
16 proposed VPCs illustrated in Fig. 2(c) reveals that the dispersion slope is virtually linear,
17 and there only exists one edge mode bounded to the valley. The dispersion relation
18 provides a potential possibility to manipulate a broadband FWM process inside the
19 topological bandgap, However, the phase-matching condition should be a major
20 consideration for enhancing the FWM interaction. In particular, the energy conversion
21 becomes more efficient when the nonlinear wavevector mismatch ($\Delta k = 2k_p - k_s -$
22 k_i) satisfies $\Delta k = 0$. By utilizing the energy conversion of FWM interactions, we
23 calculate the map of wavevector mismatch Δk of the VPC, as depicted in Fig. 3(a). It
24 is noted that the conversion efficiency of the FWM interaction increases as the
25 wavevector mismatch Δk decreases. To get the small value of wavevector mismatch
26 Δk of the map, we choose the frequencies of the nonlinear process as $\nu_p = 196.5$ THz,
27 $\nu_s = 196.9$ THz and $\nu_i = 196.1$ THz respectively. The scalar nonlinear wavevector
28 mismatch of this FWM process is calculated as $\Delta k = 1.89 \times 10^{-6}$.

1 To excite the nonlinear FWM interaction, the input field amplitudes of the pump and
2 signal are set as $|E_p| = 4 \times 10^5$ V/m and $|E_s| = 4 \times 10^4$ V/m, respectively. The
3 excitation of the idler is replaced by scattering boundary condition, which implies that
4 the input power of the idler is set as $|E_i| = 0$ V/m. The nonlinearity of silicon is
5 considered as a third-order susceptibility tensor $\chi^{(3)}$ with a constant scalar value of
6 2.45×10^{-19} m²/V².
7 Let us consider the evolution of the FWM process in the designed VPC. Field profiles
8 of the signal and idler are simulated, and the results are depicted in Fig. 3(b). It can be
9 observed that a topological valley kink state of idler frequency is excited along the
10 interface between two different VPCs, which gives evidence to the generation of the
11 FWM process. Remarkably, there is no excitation at the frequency of the idler, therefore
12 the field amplitudes of edge state at the input are almost invisible, and getting bigger
13 with the propagation in the VPCs. Moreover, the valley kink state of generated idler
14 photons is robust to the sharp bend, resulting in topological protection of idler photons
15 due to the spectral overlap of the idler and edge states.



16
17 Fig. 3 Topologically protected FWM interaction of valley kink states. (a) Map of wavevector
18 mismatch Δk of the VPC, where ν_p , ν_s and ν_i represent the frequency of pump, signal and idler
19 respectively. (b) Field profiles of the signal ($\nu_s = 196.9$ THz) and idler ($\nu_i = 196.1$ THz) along the
20 topological interface.

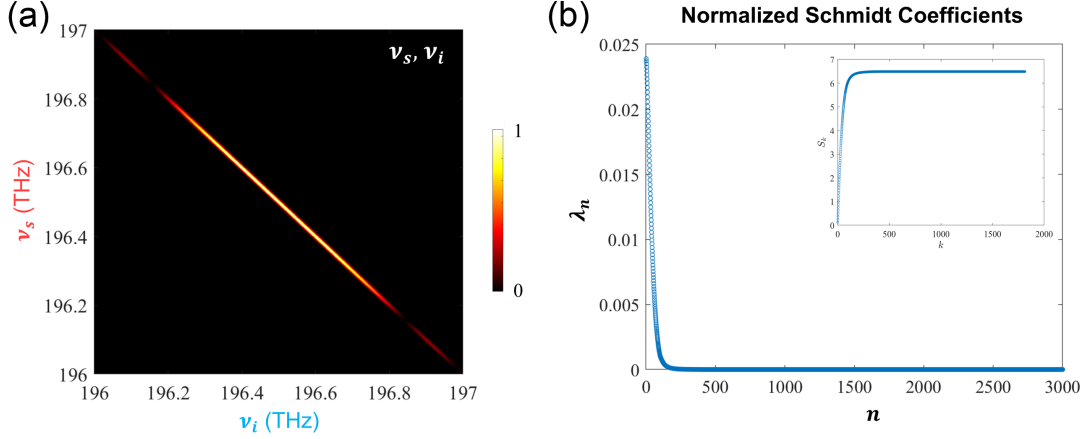
21 To theoretically calculate the continuous frequency entanglement of photon pairs
22 emerging from the FWM process, we conduct the quantum evolution of photon pairs
23 (see Supplementary Information). The biphoton state generated from nonlinear FWM
24 interaction can be written as

$$25 \quad |\Psi\rangle = \iint d\omega_s d\omega_i \mathcal{A}(\omega_s, \omega_i) \hat{a}_{\omega_s}^\dagger \hat{a}_{\omega_i}^\dagger |0\rangle, \quad (1)$$

26 where $\hat{a}_{\omega_s}^\dagger$ and $\hat{a}_{\omega_i}^\dagger$ are creation operators, and $\mathcal{A}(\omega_s, \omega_i)$ is the JSA. Consider the
27 phase-matching condition of FWM processes, the joint JSA is given by²⁷

$$28 \quad \mathcal{A}(\omega_s, \omega_i) = \alpha\left(\frac{\omega_s + \omega_i}{2}\right) \Phi(\omega_s, \omega_i), \quad (2)$$

1 where the spectrum envelope of the pump $\alpha(\frac{\omega_s+\omega_i}{2})$ and joint phase-matching
 2 spectrum $\Phi(\omega_s,\omega_i)$ are modeled approximately, with the forms of
 3 $\alpha(\frac{\omega_s+\omega_i}{2})=\delta(\omega_s+\omega_i-2\omega_p)$ and $\Phi(\omega_s,\omega_i)=\text{sinc}(\frac{\Delta kL}{2})$. The JSA describing the
 4 biphoton state amplitude function in VPCs is depicted in Fig. 4(a), gives a moderate
 5 probability of entanglement between signal and idler photons. To quantify this, the
 6 Schmidt decomposition method is employed to testify the separability of the JSA.



7
 8 Fig. 4 (a) JSA distribution of the signal and the idler in the VPCs comprising of VPC₁ and VPC₂.
 9 (b) Normalized Schmidt coefficients of photon pairs after propagation along the topological
 10 interface, the inset shows the entropy of entanglement of the system.

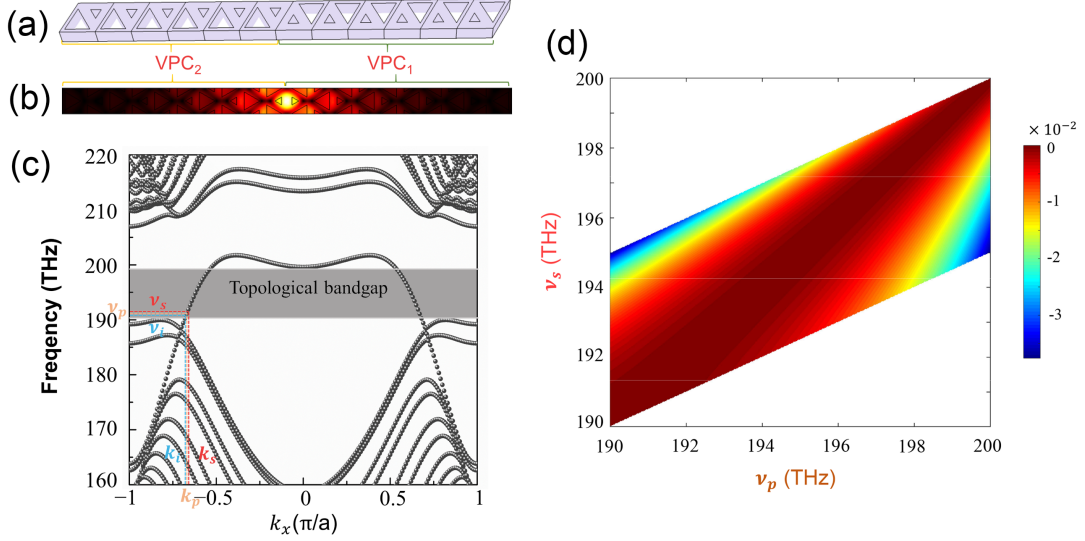
11 The normalized Schmit coefficients λ_n represents the probability of obtaining the
 12 n th biphoton state. As shown in Fig. 4(b), the number of nonzero Schmit coefficients
 13 λ_n is greater than 1, leading to clear evidence of entanglement of biphotons. The
 14 entanglement can also be described by the entropy of entanglement²⁷ with $S_k > 0$,
 15 where $S_k = -\sum_{n=1}^N \lambda_n \log_2 \lambda_n$. The inset of Fig. 4(b) demonstrates that the convergency
 16 value of entropy of entanglement is 6.49, which implies high quality of continuous
 17 frequency entanglement of biphotons in the VPCs. Furthermore, the emergence of
 18 valley kink states gives rise to the topological protection of entangled photon pairs
 19 originating from the FWM process in the VPCs.

20 Discussion

21 FWM interactions in VPCs with different interfaces

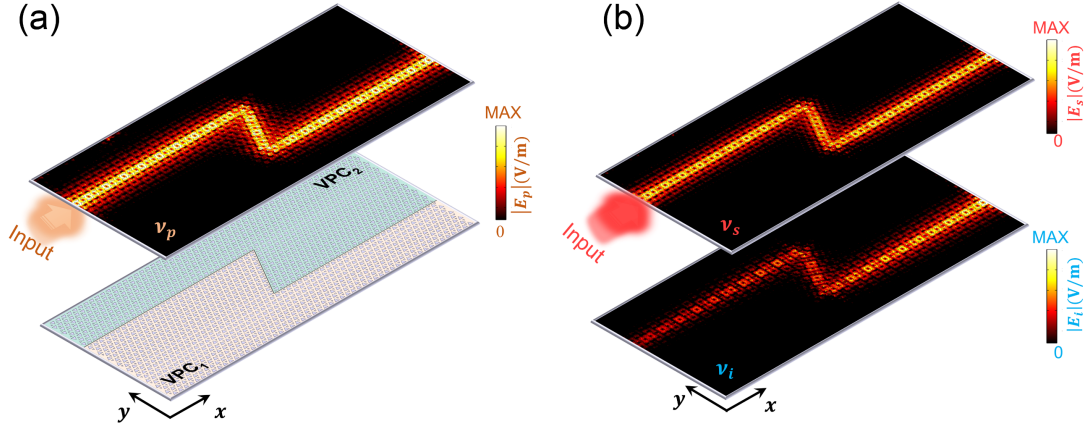
22 Carefully considering the topological behaviors of VPCs with different interfaces, we
 23 construct a photonic crystal configuration with modulating inversely the localizations
 24 of VPCs, as shown in Fig. 5(a). We perform an extensive calculation on the dispersion
 25 relation of designed VPCs. As depicted in Fig. 5(c), there exists a dispersion curve
 26 distinguished from the bulk inside the bandgap, which denotes the topological one-way
 27 edge modes along the interface. Comparing with the dispersion relation of VPCs with
 28 the first type interface (shown in Fig. 2(c)), the slopes of dispersion curves of VPCs
 29 with the second type interface exhibit opposite values owing to inversion of lattice

1 symmetry for VPCs. It is worth mentioning that bands of kink edge states in two
 2 interfaces are not perfect mirror-symmetric, which is contributed by the unrighteous
 3 symmetry of unit cells of VPCs ($d_1 \neq d_2$). We simulate the field profiles of valley kink
 4 states around the interface as illustrated in Fig. 5(b). Analogously, the map of
 5 wavevector mismatch Δk in the VPC is calculated as depicted in Fig. 5(d). Compared
 6 with the map of wavevector mismatch Δk in the VPC shown in Fig. 3(a), the relative
 7 values of wavevector mismatch Δk are larger, resulting in the lower efficiency of
 8 conversion of the FWM interaction.



9
 10 Fig. 5 Topological valley kink states in VPCs with different interfaces. (a) Schema of proposed VPC
 11 structure comprising of VPC₂ and VPC₁. (b) Simulated field profiles of the valley kink state around
 12 the interface. (c) Calculated band diagram of valley kink states in the designed VPC. (d) Map of
 13 wavevector mismatch Δk of the VPC.

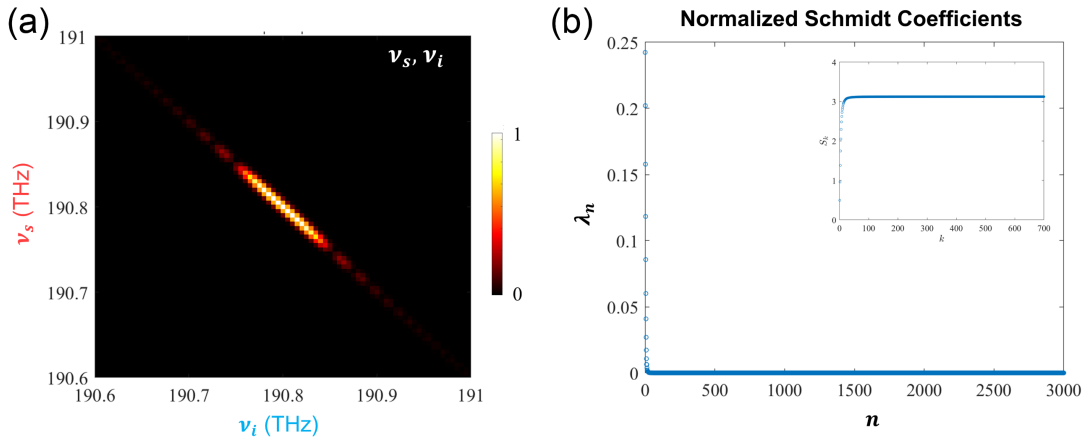
14 We study the spontaneous FWM interaction in designed VPCs with different
 15 interfaces, the frequencies of the pump, signal and idler are chosen as $\nu_p =$
 16 191.8 THz, $\nu_s = 191.9$ THz and $\nu_i = 191.7$ THz, respectively. The scalar nonlinear
 17 wavevector mismatch is calculated as $\Delta k = -8.42 \times 10^{-6}$. We perform the numerical
 18 simulations of nonlinear FWM interactions along a “Z” shaped interface between the
 19 VPC₂ and VPC₁, the field profiles of the pump along the interface are depicted in Fig.
 20 6(a). The field profiles of the signal and idler are shown in Fig. 6(b), idler photons are
 21 generated and amplified with the light propagation of edge states as a result of the
 22 emergence of the nonlinear FWM process. The valley kink states of pump, signal and
 23 idler propagating along the interface between VPC₂ and VPC₁ are robust to the sharp
 24 bends.



1

2 Fig. 6 FWM interactions in VPCs with different interfaces. (a) Field profiles of the pump ($\nu_p =$
 3 190.8 THz) along a “Z” shaped interface between the VPC₂ and VPC₁. (b) Field profiles of the
 4 signal ($\nu_s = 190.9$ THz) and idler ($\nu_i = 190.7$ THz) in the VPCs.

5 According to the map of wavevector mismatch Δk of designed VPCs, we draw the
 6 JSA of biphoton state propagating along the interface between the VPC₂ and VPC₁. As
 7 illustrated in Fig. 7(a), the joint spectrum intensity implies that the frequency
 8 correlation of the signal and idler is not strong. Large values of relative wavevector
 9 mismatch Δk lead to low efficiency of the FWM process. Analogously, the
 10 entanglement of biphotons in the VPCs comprising of VPC₂ and VPC₁ is clarified. The
 11 normalized Schmidt coefficients λ_n of biphotons is depicted in Fig. 7(b), which
 12 reveals that the biphoton state is entangled. However, comparing with the results of
 13 VPCs with the first type interface (shown in Fig. 4), the number of nonzero Schmit
 14 coefficients λ_n is small, indicating the low quality of entanglement between signal and
 15 idler photons. The wavevector mismatch Δk of the second type of VPC interface is
 16 two orders of magnitude higher than that of the first type of VPC interface shown in fig
 17 3(a), which implies that few FWM processes satisfying the phase-matching condition
 18 emerge for the second type of VPC interface. It can also be proved by bandwidth of the
 19 JSA distribution of two VPCs. For the second type of VPC interface, the dimensions of
 20 JSA $A(\omega_s, \omega_i)$ in Hilbert space are lower, therefore, the number of nonzero Schmit
 21 coefficients λ_n is smaller, resulting in lower quality of entanglement. The result is also
 22 proved by the entropy of entanglement S_k plotted in the inset of Fig. 7(b).



1 Fig. 7 (a) JSA distribution of the signal and the idler in the VPCs comprising of VPC₂ and VPC₁.
2 (b) Normalized Schmidt coefficients of biphoton states after propagation along the topological
3 interface, the inset shows the entropy of entanglement of the system.

4 **Conclusion**

5 In this work, we have demonstrated a photonic-crystal-based platform that combines
6 the topological photonic systems and entangled biphoton states. In particular, the
7 topological valley kink states propagating along the interfaces are observed in photonic
8 crystals emulating the QVH effect. Simulated transmittances of kink states confirm the
9 behaviors of topological properties, including back-scattering suppression and
10 immunity to structure imperfections. By introducing the nonlinear FWM interaction
11 into photonic systems, we conduct the generation and amplification of idler photons
12 along the interfaces between two different VPCs. We theoretically clarify that the
13 photon pairs generated from the FWM interaction are continuous frequency entangled.
14 Moreover, with the overlap between the frequencies of FWM interactions and operation
15 bandwidths of valley kink states, the one-way propagating modes of the pump, signal
16 and idler show robustness against the sharp bends and scattering, giving rise to the
17 topological protection of entangled photon pairs.

18 **Acknowledgments**

19 This work is supported by the Key-Area Research and Development Program of
20 Guangdong Province under Grant 2018B030325002, the National Natural Science
21 Foundation of China (Grant Nos. 62075129, 61975119).

22 **Conflict of interest**

23 The authors declare that they have no conflict of interest.

24 **Methods**

25 **Numerical Modeling**

26 We use the finite-element method solver COMSOL Multiphysics to conduct numerical
27 simulations of topological photonic crystals. The material of photonic crystals is chosen
28 as silicon due to the extensive application and high third-order nonlinearity $\chi^{(3)}$. For
29 simplified calculation, the refractive index of silicon is performed as $n_{Si}=2.965$ in two-
30 dimensional configuration^{16,28}. We also prove that topological protected entangled
31 photon pairs can be achieved even consider the material dispersion of silicon.

32 In this case, we consider the topological behavior of transverse electric polarization
33 modes in the VPCs. We have simulated the field profiles of topological valley kink
34 states in the VPCs with a source $E_p = E_x + iE_y$ that emulates a right circularly
35 polarized light. The circular polarizations of the source are analogous to the
36 pseudospins in the QSH systems^{6,29-32}. Two detector dipoles are set around the input
37 and output port along the “Z” shaped interface to calculate the transmittances of kink
38 states.

39 To perform the nonlinear elements in the VPCs, the third-order nonlinearity of silicon
40 $\chi^{(3)}$ is identified by a constant scalar value³³ of $2.45 \times 10^{-19} \text{ m}^2/\text{V}^2$. The FWM

1 interaction is conducted by the third-order nonlinear polarization of silicon, which is
2 described by

$$3 \quad \mathbf{P}_p(\omega_s + \omega_i - \omega_p) = 6\varepsilon_0\chi^{(3)}E_sE_iE_p^*, \quad (3)$$

$$4 \quad \mathbf{P}_s(\omega_p + \omega_p - \omega_i) = 3\varepsilon_0\chi^{(3)}E_pE_pE_i^*, \quad (4)$$

$$5 \quad \mathbf{P}_i(\omega_p + \omega_p - \omega_s) = 3\varepsilon_0\chi^{(3)}E_pE_pE_s^*, \quad (5)$$

6 where $\mathbf{P}_{p,s,i}$ and $E_{p,s,i}$ are the polarization and electric field of the pump, signal and
7 idler. In the simulations, the input field amplitudes of the pump and signal are set as

8 $|E_p| = 4 \times 10^5$ V/m and $|E_s| = 4 \times 10^4$ V/m, respectively. The input electric field

9 amplitude of the idler is set as $|E_i| = 0$ V/m, then the excitation of model at the idler
10 frequency is driven by the nonlinear coupling of electromagnetic models at the pump
11 and signal frequencies. Therefore, the generation of edge modes at the idler frequency
12 implies the emergence of the nonlinear FWM interaction. A left-handed circularly
13 polarized source is applied to excite pseudospin down (σ^-) states at the frequencies of
14 the pump and signal, however, there is no input for the idler. Hence, the

15

16 **Hamiltonian of FWM interaction**

17 The nonlinear FWM interaction is generated in the VPCs due to the third-order
18 nonlinearity of silicon $\chi^{(3)}$. It is noted that the Hamiltonian governing FWM
19 interaction is described by

$$20 \quad H = H_L + H_{NL}, \quad (6)$$

21 where^{20,21,34}

$$22 \quad H_L = \sum_j \int d\omega_j \hbar\omega_j a_{j,\omega_j}^\dagger a_{j,\omega_j}, \quad (7)$$

$$23 \quad H_{NL} = -\gamma_0 \int d\omega_p d\omega_s d\omega_i a_{p,\omega_p}^\dagger a_{p,\omega_p}^\dagger a_{s,\omega_s} a_{i,\omega_i} e^{i(2k_p - k_s - k_i)x} + h.c., \quad (8)$$

24 with γ_0 is effective nonlinear coupling constant, a_m^\dagger is the creation operator of the
25 pump, signal and idler photons represented by $\mu \in \{p, s, i\}$.

26

References

- 1 F. Haldane & S. Raghu. Possible realization of directional optical waveguides in photonic crystals with broken time-reversal symmetry. *Phys. Rev. Lett.* **100**, 013904 (2008).
- 2 S. Raghu & F. D. M. Haldane. Analogs of quantum-Hall-effect edge states in photonic crystals. *Phys. Rev. A* **78**, 033834 (2008).
- 3 M. Hafezi, S. Mittal, J. Fan, A. Migdall & J. Taylor. Imaging topological edge states in silicon photonics. *Nat. Photon.* **7**, 1001-1005 (2013).
- 4 A. Slobozhanyuk, S. H. Mousavi, X. Ni *et al.* Three-dimensional all-dielectric photonic topological insulator. *Nat. Photon.* **11**, 130-136 (2017).
- 5 X. Cheng, C. Jouvaud, X. Ni *et al.* Robust reconfigurable electromagnetic pathways within a photonic topological insulator. *Nat. Mater.* **15**, 542-548 (2016).
- 6 L.-H. Wu & X. Hu. Scheme for achieving a topological photonic crystal by using dielectric material. *Phys. Rev. Lett.* **114**, 223901 (2015).
- 7 M. A. Gorlach, X. Ni, D. A. Smirnova *et al.* Far-field probing of leaky topological states in all-dielectric metasurfaces. *Nat. Commun* **9**, 1-8 (2018).
- 8 N. Parappurath, F. Alpeggiani, L. Kuipers & E. Verhagen. Direct observation of topological edge states in silicon photonic crystals: Spin, dispersion, and chiral routing. *Sci. Adv.* **6**, eaaw4137 (2020).
- 9 F. Gao, H. Xue, Z. Yang *et al.* Topologically protected refraction of robust kink states in valley photonic crystals. *Nat. Phys.* **14**, 140-144 (2018).
- 10 X.-T. He, E.-T. Liang, J.-J. Yuan *et al.* A silicon-on-insulator slab for topological valley transport. *Nat. Commun* **10**, 1-9 (2019).
- 11 J.-W. Dong, X.-D. Chen, H. Zhu, Y. Wang & X. Zhang. Valley photonic crystals for control of spin and topology. *Nat. Mater.* **16**, 298-302 (2017).
- 12 X. Wu, Y. Meng, J. Tian *et al.* Direct observation of valley-polarized topological edge states in designer surface plasmon crystals. *Nat. Commun* **8**, 1-9 (2017).
- 13 S. Arora, T. Bauer, R. Barczyk, E. Verhagen & L. Kuipers. Direct quantification of topological protection in symmetry-protected photonic edge states at telecom wavelengths. *Light Sci. Appl.* **10**, 1-7 (2021).
- 14 D. Smirnova, A. Tripathi, S. Kruk *et al.* Room-temperature lasing from nanophotonic topological cavities. *Light Sci. Appl.* **9**, 1-8 (2020).
- 15 Y. Yang, Y. Yamagami, X. Yu *et al.* Terahertz topological photonics for on-chip communication. *Nat. Photon.* **14**, 446-451 (2020).
- 16 M. I. Shalaev, W. Walasik, A. Tsukernik, Y. Xu & N. M. Litchinitser. Robust topologically protected transport in photonic crystals at telecommunication wavelengths. *Nat. Nanotechnol.* **14**, 31-34 (2019).
- 17 W. Noh, H. Nasari, H.-M. Kim *et al.* Experimental demonstration of single-mode topological valley-Hall lasing at telecommunication wavelength controlled by the degree of asymmetry. *Opt. Lett.* **45**, 4108-4111 (2020).
- 18 D. Smirnova, S. Kruk, D. Leykam *et al.* Third-harmonic generation in photonic topological metasurfaces. *Phys. Rev. Lett.* **123**, 103901 (2019).
- 19 J. W. You, Z. Lan & N. C. Panoiu. Four-wave mixing of topological edge plasmons in graphene metasurfaces. *Sci. Adv.* **6**, eaaz3910 (2020).
- 20 S. Mittal, E. A. Goldschmidt & M. Hafezi. A topological source of quantum light. *Nature* **561**,

- 1 502-506 (2018).
- 2 21 S. Barik, A. Karasahin, C. Flower *et al.* A topological quantum optics interface. *Science* **359**,
3 666-668 (2018).
- 4 22 A. Blanco-Redondo, B. Bell, D. Oren, B. J. Eggleton & M. Segev. Topological protection of
5 biphoton states. *Science* **362**, 568-571 (2018).
- 6 23 Y. Wang, X.-L. Pang, Y.-H. Lu *et al.* Topological protection of two-photon quantum correlation
7 on a photonic chip. *Optica* **6**, 955-960 (2019).
- 8 24 [Y. Chen, X.-T. He, Y.-J. Cheng *et al.* Topologically protected valley-dependent quantum
9 photonic circuits. *Phys. Rev. Lett.* **126**, 230503 \(2021\).](#)
- 10 25 M. Wang, C. Doyle, B. Bell *et al.* Topologically protected entangled photonic states.
11 *Nanophotonics* **8**, 1327-1335 (2019).
- 12 26 L. Zhang, Y. Yang, M. He *et al.* Valley kink states and topological channel intersections in
13 substrate-integrated photonic circuitry. *Laser Photonics Rev.* **13**, 1900159 (2019).
- 14 27 C. Law, I. A. Walmsley & J. Eberly. Continuous frequency entanglement: effective finite
15 Hilbert space and entropy control. *Phys. Rev. Lett.* **84**, 5304 (2000).
- 16 28 M. Hammer & O. V. Ivanova. Effective index approximations of photonic crystal slabs: a 2-
17 to-1-D assessment. *Opt. Quantum Electron.* **41**, 267-283 (2009).
- 18 29 W. Liu, M. Hwang, Z. Ji *et al.* Z2 photonic topological insulators in the visible wavelength
19 range for robust nanoscale photonics. *Nano Lett.* **20**, 1329-1335 (2020).
- 20 30 X. Ni, D. Purtseladze, D. A. Smirnova *et al.* Spin-and valley-polarized one-way Klein
21 tunneling in photonic topological insulators. *Sci. Adv.* **4**, eaap8802 (2018).
- 22 31 Z.-K. Shao, H.-Z. Chen, S. Wang *et al.* A high-performance topological bulk laser based on
23 band-inversion-induced reflection. *Nat. Nanotechnol.* **15**, 67-72 (2020).
- 24 32 W. Liu, Z. Ji, Y. Wang *et al.* Generation of helical topological exciton-polaritons. *Science* **370**,
25 600-604 (2020).
- 26 33 L. Wang, S. Kruk, K. Koshelev *et al.* Nonlinear wavefront control with all-dielectric
27 metasurfaces. *Nano Lett.* **18**, 3978-3984 (2018).
- 28 34 J. W. Silverstone, D. Bonneau, K. Ohira *et al.* On-chip quantum interference between silicon
29 photon-pair sources. *Nat. Photon.* **8**, 104-108 (2014).
- 30
- 31